

# Experimental investigation on the effect of granulation moisture on the flame front propagation and pore structure in the high-temperature zone of the sinter bed

Hao Zhou <sup>\*</sup>, Hanxiao Meng, Pengnan Ma, Jiankang Wang, Fangzheng Cheng, Hao Fang

State Key Laboratory of Clean Energy Utilization, Institute for Thermal Power Engineering, Zhejiang University, Hangzhou 310027, PR China

## ARTICLE INFO

### Article history:

Received 23 August 2021

Received in revised form 8 November 2021

Accepted 9 November 2021

Available online 14 November 2021

### Keywords:

Iron ore sintering

Granulation moisture

Pore structure

High-temperature zone

## ABSTRACT

The pore structure in the high-temperature zone plays a leading role in the permeability of the sinter bed. However, few studies on the bed structure in the high-temperature zone of sintering are due to the difficulty of sampling. Pilot-scale sinter pot tests were conducted to investigate the flame front propagation properties and pore evolution characteristics under different granulation moisture in this paper. Liquid nitrogen was injected to quench the sintering bed. We use X-ray computed tomography to reconstruct the high-temperature zone sinter structures. Results show that the higher porosity of green bed under higher granulation moisture results in faster flame front and more likely channels formation. The porosity of the high-temperature zone increases from 48.40% to 51.50% and 55.68% with moisture increasing from 5.30% to 6.35% and 6.91%. However, the mean length of pores decreases from 1.60 mm to 1.38 mm caused by inadequate coalesce under high moisture conditions.

© 2021 Elsevier B.V. All rights reserved.

## 1. Introduction

The iron ore sintering process is widely used globally for agglomeration of iron ore as an important pre-process of blast furnace ironmaking [1]. Iron ores, fluxes, return fines, and coke are blended before granulating with calculated water and then filled into the sinter pot [2]. After the igniter ignites, the self-sustaining porous medium combustion generates under the suction of the induced draft fan. As a typical porous media combustion process with solid fuel embedded, the iron ore sintering process is different because the solid phase participates in the reaction, and the porosity changes before and after the flame front arrive [3]. During the iron ore sintering process, the solid phases, including iron ores, fluxes, return fines, and fuel, react together. The melting processes, liquid phase generation and seepage, bubbles movement and coalescence occur [4,5]. The permeability and pore properties of the bed change significantly before and after the flame front passes through [6,7].

Previous studies divided the sintering bed into sintered zone, high-temperature zone, and humidified zone according to the sintering state of the bed materials [8]. The high-temperature zone plays a controlling role in the overall permeability of the sinter bed [8–10]. Moreover, the amount of melt formed is crucial to the agglomeration

structure and strength of the sinter [11]. Therefore, the high-temperature zone pore structure and dynamic evolution characteristics have an important influence on the permeability of the sintering bed, thus affecting the sinter yield, productivity, and strength [12]. It is clear that the structure of the green bed will affect the structure of the sinter bed. It is reported that the permeability of the sinter bed is positively related to that of the green bed [13,14]. Many factors are affecting the porosity of the green bed. Different iron ores have different absorption and infiltration of water, and their bonding properties are also different [15]. Raw material particles with different structures, sizes and strengths prepared by different granulation processes also affect the structure of the green bed [16–18]. The porosity of the green bed layer under different bed heights is different because of the compaction effect caused by gravity load [19–21]. Granulation moisture is also one of the critical factors affecting the structure of the green bed. The particle size of raw materials increases and its distribution narrows, the permeability of the green bed increases, thus the flame front speed increases [22], with the increase of granulation moisture within a specific critical value range, which is different for different iron ore materials [23,24]. The permeability of the green bed deteriorates under the condition of too high granulation moisture [25]. Moisture transfer between bed layers caused by evaporation and condensation also changes the bed structure and permeability during sintering [26]. According to the existing state of water in the sintering process, Podder [27] divided the unsintered region into four regions: drying region, equilibrium zone, condensation zone, and unreacted zone. With the sintering

<sup>\*</sup> Corresponding author.

E-mail address: [zhouhao@zju.edu.cn](mailto:zhouhao@zju.edu.cn) (H. Zhou).

**Table 1**  
Ore blend and sinter mix proportioning.

Basic ore blend proportion (wt% ore basis)		
Australia ore A		16.67
Australia ore B		16.67
Australia ore C		33.33
Brazil ore A		16.67
Brazil ore B		16.67
Sinter mix proportioning (wt% ore basis)		
Basic ore blend		57.48
Limestone		8.08
Dolomite		4.94
Coke breeze		4.50
Return fines	3.35–5.00 mm	16.67
	0–3.35 mm	8.33

process, the bed state continues to transform, and the position of different zones is also changing, which affects the airflow through the bed. Thus, it is of great significance to study the structure change of the sintering bed, especially the high-temperature zone, and its influence on the flame propagation under different granulation moisture for optimizing the sintering quality and yield.

X-ray computed tomography (XCT) has been widely used to analyze the pore characteristics of porous media with the development of spatial visualization techniques and numerical modeling methods since recent decades [28,29]. The non-destructive scanning and model reconstruction of the sinter can be realized using XCT, which can effectively reproduce the three-dimensional (3D) pore structure of the sinter and better analyze the pore characteristics. Nushiro et al. [30] put a small sinter pot in the center of the XCT device and obtained the pore structure of the sinter with different bulk densities of raw materials. Nevertheless, only millimeter-sized pores were analyzed, limited to the equipment conditions at that time. Shatokha et al. [31] proposed a method to distinguish open and closed pores of sinter and analyze their pore characteristics using XCT data, which realized a wider range of pore size measurement than mercury intrusion porosimetry to measure a higher open porosity. XCT can also reveal the volumetric spatial distribution of the pores, which cannot be obtained from traditional techniques such as mercury intrusion porosimetry and optical microscopy [32]. Zhou et al. [16] reconstructed clear pore distribution and topology by applying XCT and numerically analyzed the pore characteristics and permeability of several raw materials packed beds. However, most of the researches on the pore characteristics of sinter use the sintered samples [7,14,33] or the tablets made of ore powder to simulate the sintering samples [34] for XCT analysis due to the difficulty of sampling the high-temperature zone under sintering.

**Table 2**  
Sintering conditions.

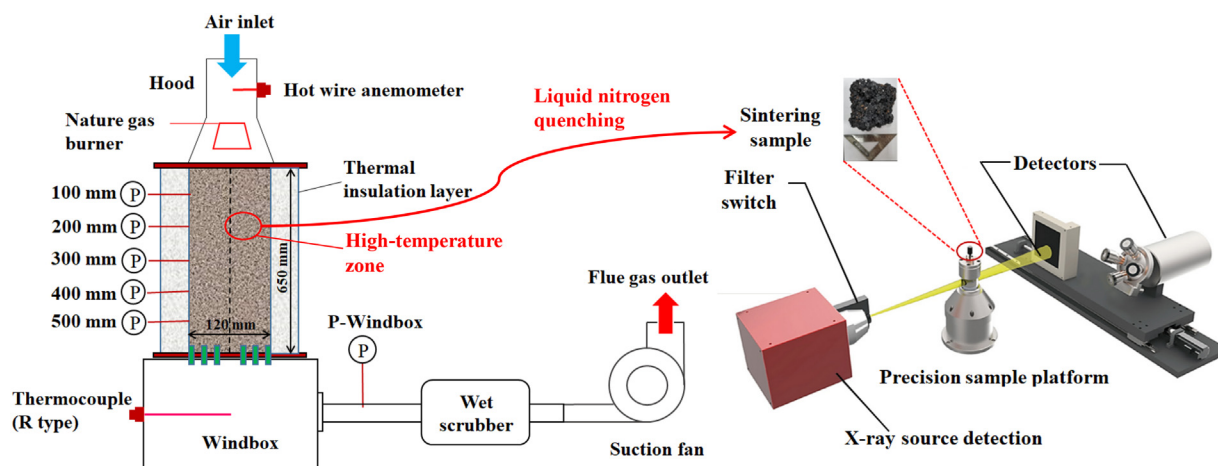
Sintering conditions		
Bed height (mm)		650
Ignition suction (kPa)		6
Ignition temperature (°C)		1200
Ignition time (s)		90
Sintering suction (kPa)		16
Moisture (wt%)	Case1	5.30
	Case2	6.35
	Case3	6.91

The liquid nitrogen quenching method has been used in previous studies. Zhao et al. and Zhou et al. [35–37] froze the sintering raw materials after granulation with liquid nitrogen in order to make the particles firm without changing the particle size of the raw materials, so as to be used for screening and particle size analysis. Pownceby et al. [38,39] quenched micro simulated sintered sample to investigate the solid solution range, thermal stability, and selected phase relationships of silico-ferrite of calcium and aluminum (SFCA). Berg et al. [40] injected liquid nitrogen into a 400 mm high sinter pot to quench the high-temperature sinter to analyze the effect of oxygen potential change on the metallographic composition of the sinter. However, the height of the sintering bed has a significant impact on the gravity load of the bed and the heat storage effect in the sintering process, affecting the pore structure of the sintering bed. In this study, liquid nitrogen was used to rapidly quench a 650 mm sintering bed, which is closer to the height of industrial sintering machines, to preserve the high-temperature zone structure since sintering. Then XCT was applied to reconstruct the complete three-dimensional structure of samples in the high-temperature zone. The number, distribution and morphological characteristics of pores were extracted to evaluate the effect of granulation moisture on the structure of the high-temperature zone under sintering.

## 2. Experimental

### 2.1. Materials and sinter pot test

Table 1 shows the materials of this study and their proportioning, including a mixture of three Australian ores and two Brazilian ores, coke, limestone, dolomite, and return fines, according to the typical iron ore proportioning in the Asia Pacific region. The binary basicity, defined as the ratio of CaO and SiO<sub>2</sub> mass content in the mixture, is mainly controlled by adding flux, including limestone and dolomite. Of course, the addition of return fines and coke breeze will also affect

**Fig. 1.** Procedures of sinter pot tests and X-ray computed tomography system.

the basicity. The proportion of each raw material is comprehensively adjusted to ensure that the binary basicity is 1.90. The particle sizes of ore, coke and flux shall not exceed 10 mm, 5 mm and 3 mm, respectively. The addition of return fines with the particle size of 0–3.35 mm and 3.35–5 mm is controlled in the ratio of 1:2, so that the return fines ratio of the total sintering mixture is 25.00%. The coke ratio of 4.50% is suitable for this ingredient according to our previous experimental [41]. The raw materials preliminarily mixed according to Table 1 were put into the drum for 1 min dry mixing and then 10 min wet mixing with calculated water addition.

The procedures of the sinter pot tests are shown in Fig. 1, and the sinter condition is shown in Table 2. The granules are filled into a 650 mm high cylindrical sintering pot with an inner diameter of 120 mm, which was paved with 1 kg sinters with a particle size of 6.3–8 mm at the bottom in advance. Under the wind box negative pressure of 6 kPa, a 50–100 mm thick flame front is formed after a 90 s ignition with natural gas igniter. Then the flame front propagates from top to bottom along the bed under the suction of the induced draft fan as the negative pressure of the wind box was increased to 16 kPa rapidly. Five pressure sensors are installed on the sintering cup 100 mm, 200 mm, 300 mm, 400 mm, and 500 mm from top to bottom to measure the change of bed layer pressure during sintering.

Three sinter pot tests were conducted to investigate the influence of granulation moisture (5.30%, 6.35%, 6.91%) on high-temperature zone pore structure and flame propagation characteristics of the sintering bed, as shown in Table 2. According to the indication of pressure sensors, it was considered that the sintering process was half-finished when the negative pressure of the bed layer at 300 mm decreased rapidly, which indicated that the flame front was passing through the bed layer at 300 mm. The induced draft fan was shut off and the liquid nitrogen was injected for rapid cooling and then sampling the sinter. The cylindrical sinter samples from the high-temperature zone with both diameter and height of 100 mm were scanned using XCT. The current and voltage of XCT were set to 350  $\mu$ A and 190 kV. The samples were placed 510 mm and 860 mm away from the X-ray source and detectors,

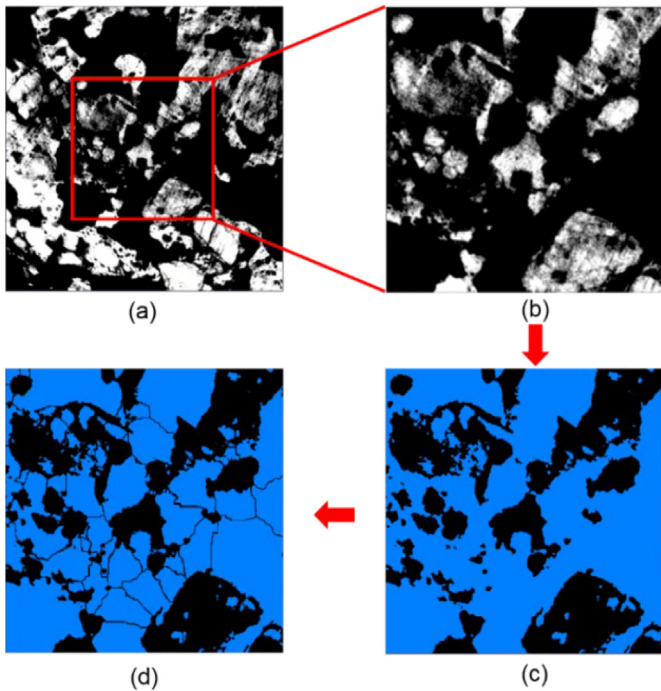


Fig. 2. XCT images processing procedure: (a) original XCT image; (b) selection of region of interest (ROI); (c) noise reduction and binarization (blue: pore, black: void); (d) segmentation.

respectively. The exposure time was set to 0.8 s. Considering the limitation of computing resources and the balance of accuracy requirements, we selected the resolution to 74  $\mu$ m which can capture most of the pores in the sinter and effectively evaluate the permeability of the sinter bed but not exceed the bearing range of computing resources.

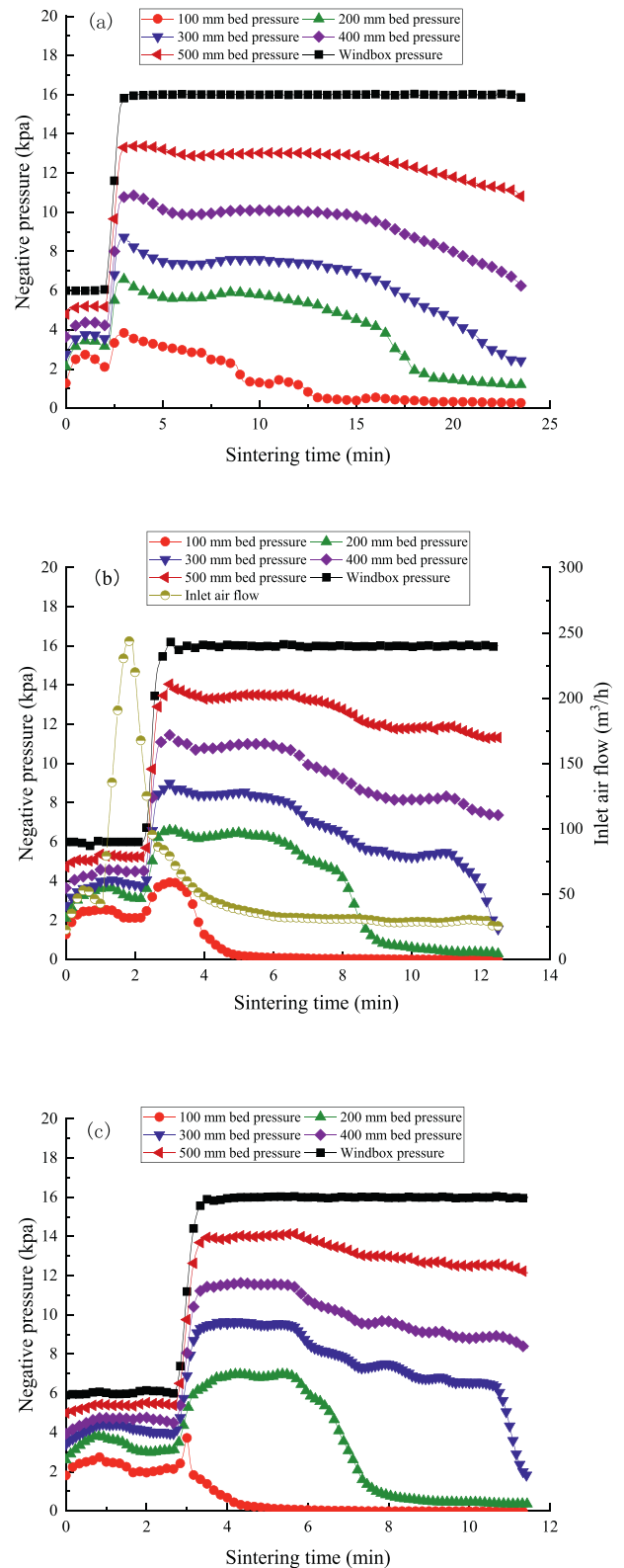


Fig. 3. Distribution of negative pressure of sintering bed under different granulation moisture, (a) 5.3%, (b) 6.35%, (c) 6.91%.

## 2.2. X-ray computed tomography image processing

The 3D reconstruction of the sinter structure and the calculation of pore parameters need a lot of computing resources. As we all know, the particle size of sinter in industrial production is 5–40  $\mu\text{m}$  and the boundary of “macropore” and “micropore” is usually 1  $\mu\text{m}$  in most studies on pore analysis of sinter [41]. So a  $30 \times 30 \times 30 \text{ mm}^3$  cube region was extracted from the scanned samples for calculation and parameter statistics in this study, which is enough to characterize the sinter, considering the trade-off between calculation resource consumption and analysis accuracy.

Fig. 2 shows the typical images processing procedure of the XCT slice. Fig. 2(a) is a typical XCT slice grayscale image. Firstly, a  $30 \times 30 \times 30 \text{ mm}^3$  region of interest (ROI) was extracted from the original XCT data (Fig. 2(b)). Secondly, noise reduction and binarization of the ROI grayscale image were carried out (Fig. 2(c)) to distinguish the pore and solid matrix. Then the binary slices were segmented (Fig. 2

(d)) to count the parameters such as equivalent diameter and sphericity of pores.

The spherical equivalent diameter  $D_e$  of the pore was defined as eq. (1):

$$D_e = \sqrt[3]{\frac{6V}{\pi}} \quad (1)$$

The sphericity of pores was defined as eq. (2):

$$\psi = \frac{\sqrt[3]{\pi(6V)^2}}{S} \quad (2)$$

Where  $V$  is the volume of pores ( $\text{m}^3$ ) and  $S$  is the area of pores ( $\text{m}^2$ ).

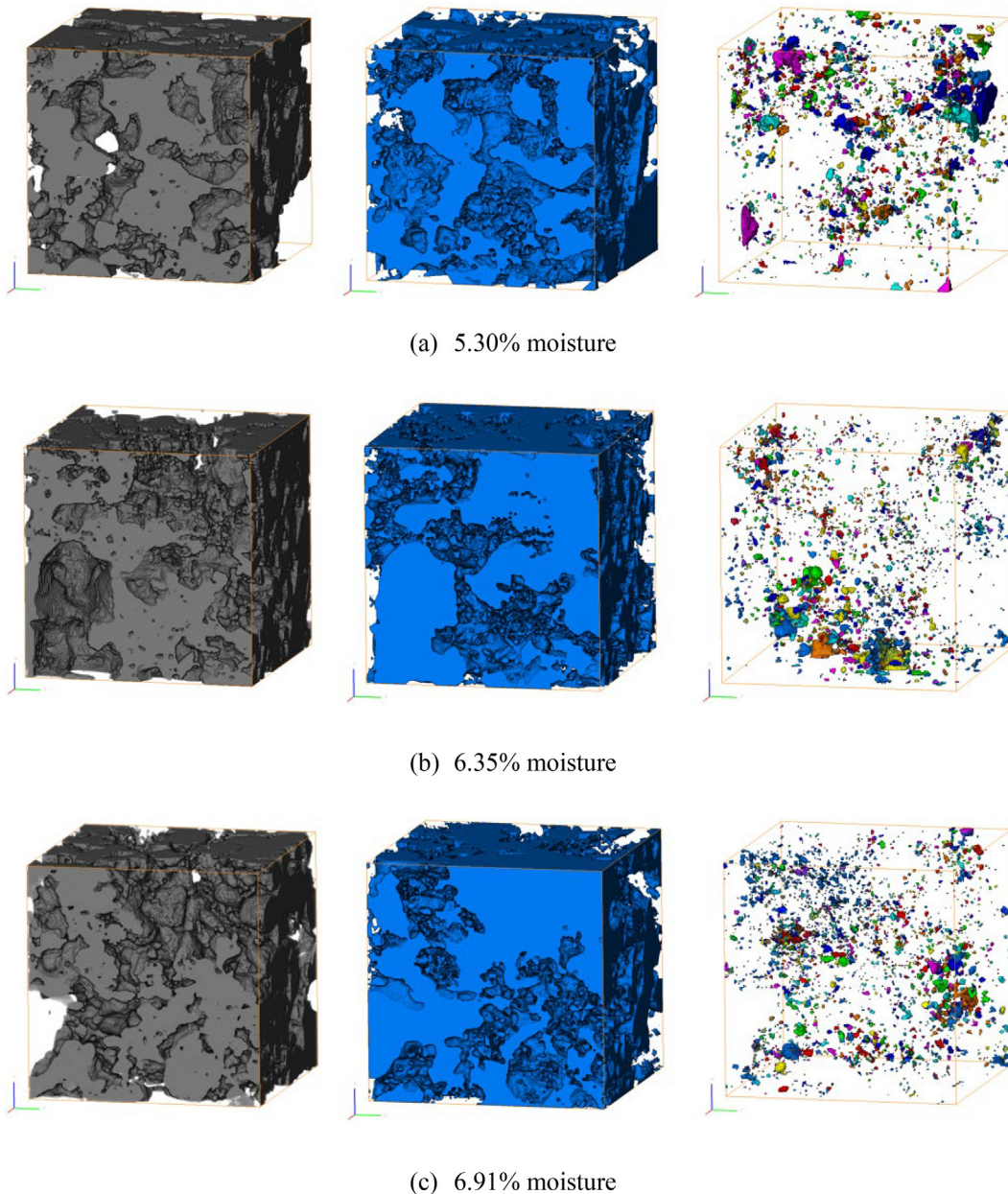


Fig. 4. 3D structure of solid matrices and pores (left: solid matrix, middle: pore structure, right: closed pores).

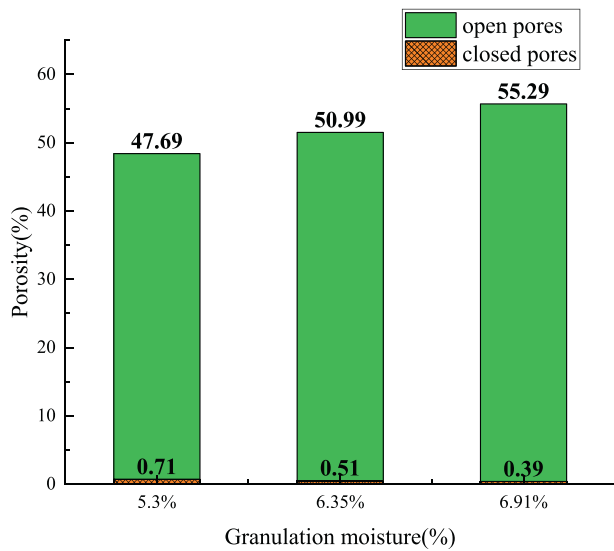


Fig. 5. The volume fractions open pores and closed pores in the high-temperature zone under different granulation moisture.

### 3. Results and discussion

#### 3.1. Flame front propagation characteristics of the sinter bed

The pressure drop in the sintering process is mainly caused by the high-temperature zone [9]. In a typical iron ore sintering process, the bed negative pressure increased gradually from top to bottom. At a certain height, the decrease of the bed negative pressure is slight before the flame front reaches but rapid when the flame front leaves. In order to monitor the flame front propagation process, pressure sensors were used to monitor the pressure changes at different bed heights during sintering. Fig. 3 shows the bed pressure curves under three different granulation moisture conditions during sintering. Before the start of sintering, the negative pressure of the wind box was increased to 16 kPa after 90 seconds of ignition at a low negative pressure of 6 kPa. Therefore, it is considered that the surge of negative pressure of wind box to 16 kPa is the sign of the start of sintering.

The quotient of the sinter bed height divided by the sintering time is the flame front speed. Under the condition of 5.30% moisture, the flame front speed is low, and the pressure drops slowly due to the lousy

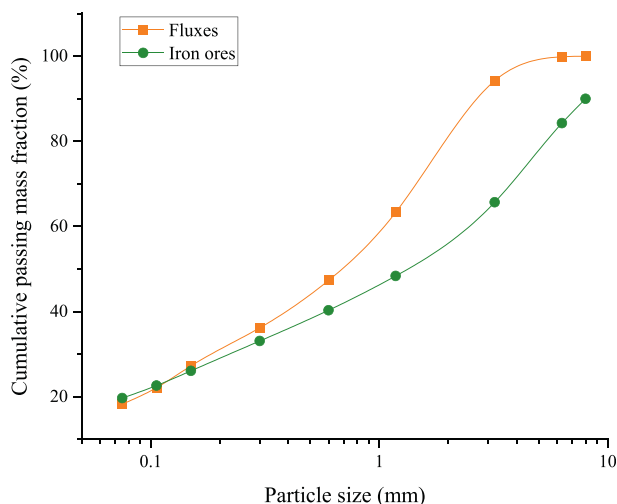


Fig. 6. Particle size distribution of sinter mixture.

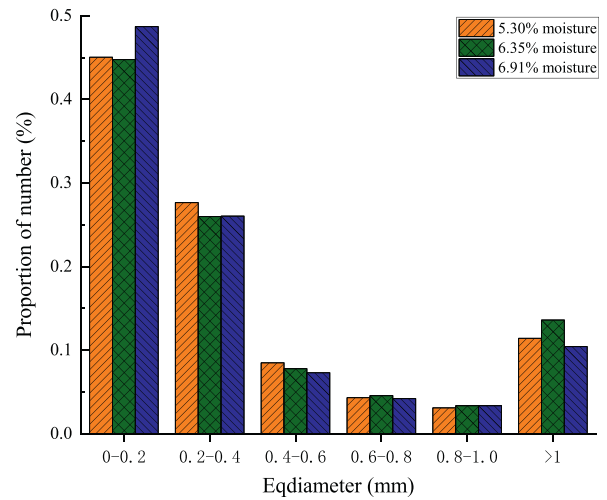


Fig. 7. Proportion of pore number under different moisture.

permeability of the bed. With the increase of granulation moisture, the moment of rapid decrease of bed negative pressure is advanced, and the decrease speed gets faster. It indicates that the permeability of the sinter bed and the flame front speed increases with the increase of moisture. The high-temperature zone reaches a specific height bed earlier, and the duration gets shorter. The permeability-moisture curve is parabolic [9]. In the granulation process, the fine particles adhere to the large particles as the core under the action of water to form an internal initial layer. When the water is sufficient, a thicker internal initial layer will be formed, and then medium-sized particles will be embedded into the surface of the internal initial layer to form an external adhering layer. However, when the water is insufficient, these medium-sized particles are not easy to adhere or fall off after adhesion, and then scatter in the pores of the raw material bed, which is also one of the reasons for the poor permeability of the raw material bed under low moisture [9].

With the increase of granulation moisture, the formed internal initial layer is more cohesive, so more medium-sized particles are embedded to form a thicker external adhesive layer, increasing the Sauter mean diameter of raw material particles, and increasing the porosity and permeability of the green bed. However, too thick adhering layer is easy

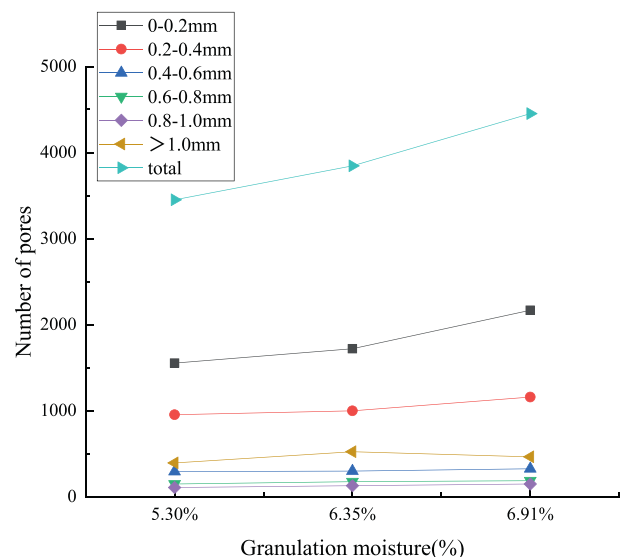


Fig. 8. Change of pore number under different moisture.

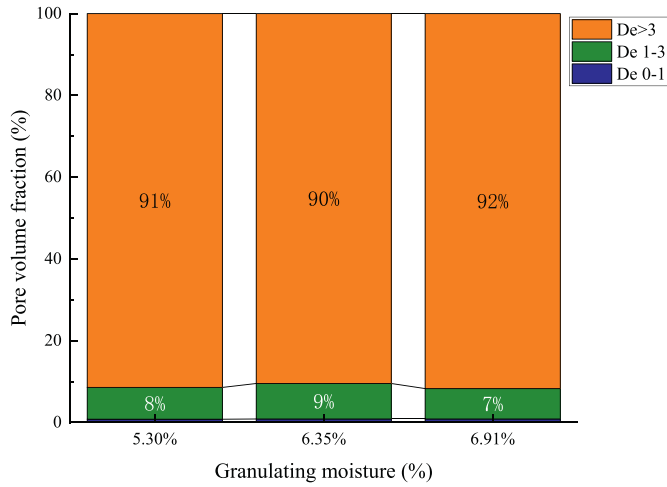


Fig. 9. The volume fraction of pores with different sizes.

to disintegrate during the filling process when the moisture exceeds a specific critical moisture value, resulting in the fine particles scattering and filling the pores of the bed, which reduce the permeability of the green bed. However, it is evident that the granulation moisture in this study did not exceed the critical value [16]. The increase of granulation moisture had a positive effect on both bed permeability and flame front speed.

### 3.2. Three-dimensional reconstruction and pore distribution of high-temperature zone structure

In order to study the structural characteristics of the high-temperature zone in the sintering process, XCT was conducted on the high-temperature zone samples cooled by liquid nitrogen under different granulation moisture sintering conditions. Then the three-dimensional reconstruction of its complete structure was carried out, as shown in Fig. 4. The pores connected with external space were defined as open pores, the pores not connected with external space were defined as closed pores, and the non-porous parts, including solid phase and solidified liquid phase, were described as matrix [31]. From left to right, the distribution of matrix, pores, and closed pores are shown in Fig. 4.

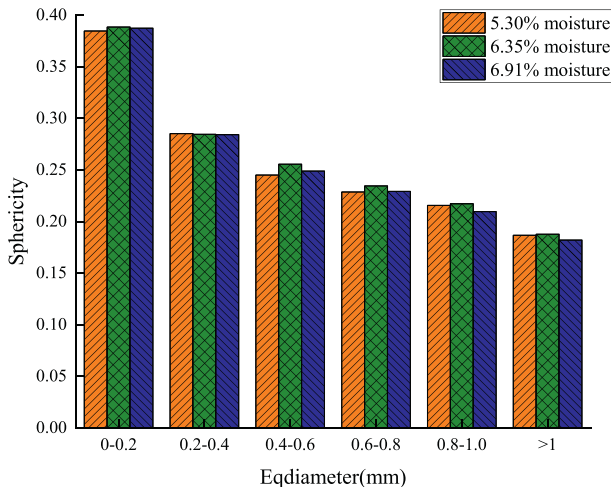


Fig. 10. Pore sphericity under different moisture.

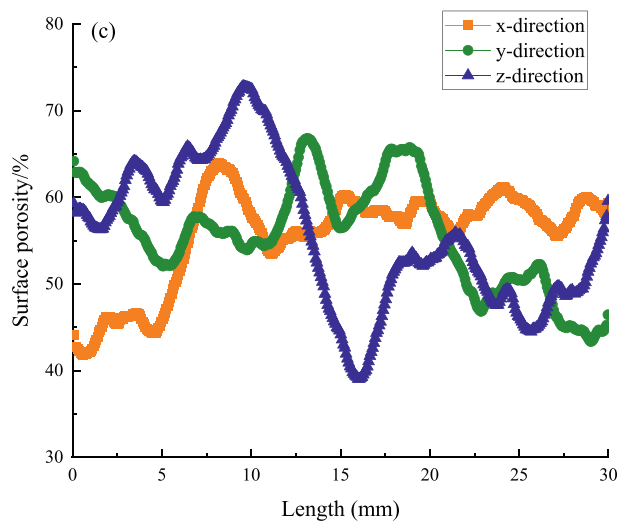
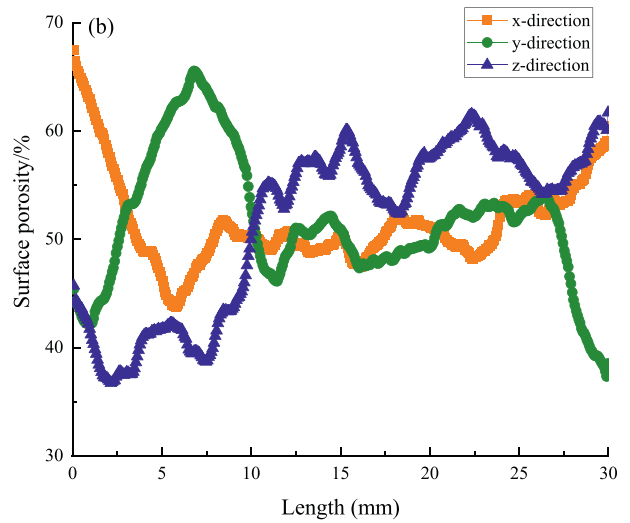
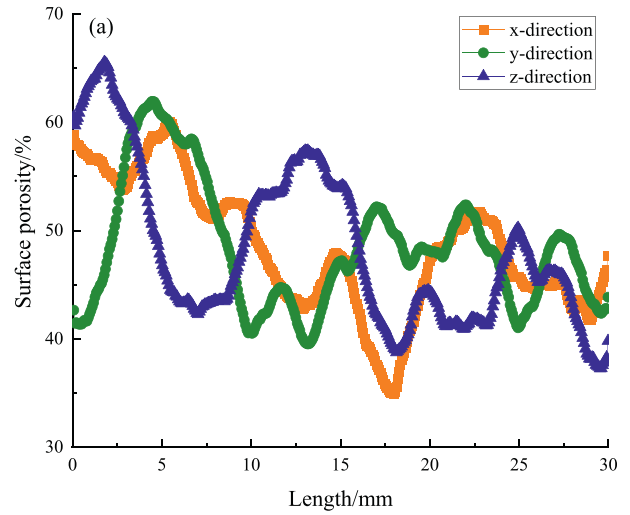


Fig. 11. Surface porosity in different directions under different moisture, (a) 5.3%, (b) 6.35%, (c) 6.91%.

Fig. 5 shows the volume fractions of open and closed pores in the high-temperature zone samples under different moisture conditions. Under the conditions of granulation moisture of 5.30%, 6.35% and 6.91%, the total porosity of samples in the high-temperature zone is 48.40%, 51.50% and 55.68%, respectively. The pore structure of the green bed is the basis of the pore structure of the sintering bed. A series of physical and chemical reactions will happen when the flame front arrives, leading to the melting and coalescence of materials. The porosity of the sinter bed is often higher than that of the green bed due to the mass loss mainly caused by fuel combustion, water evaporation, and carbonate decomposition. The change of pore morphology and distribution primarily occurs in the high-temperature zone, mainly due to the merging of small bubbles, the breaking and escaping of large bubbles, and the impact of gas flow on the liquid phase. Zhou et al. [14] reported that generally, the permeability of the sinter bed is positively correlated with that of the green bed. The variation trend of the sintering bed porosity in the high-temperature zone is also consistent with the green bed porosity. As discussed in Section 3.1, the increase of granulation moisture will increase raw material particle size, promoting the porosity and permeability of the green bed. More moisture will evaporate during sintering, resulting in more significant mass loss and further increase of bed porosity under the condition of high granulation moisture. As the transition stage between the raw bed and the sintering bed, the porosity of the high-temperature zone also increases.

In addition, as shown in Fig. 5, the volume fraction of closed pores in the high-temperature zone gradually decreases from 0.71% to 0.51% and 0.39% with the increase of granulation moisture. The increase of the high-temperature zone porosity is the superposition result of both the increase of open pore volume fraction and the decrease of pore volume fraction. The porosity of the green bed is high, and the gas flow travels faster under high moisture, as discussed in Section 3.1, so it is easier to impact the liquid phase and form the gas flow channels.

Meanwhile, the increase of quasi-particle size under high granulation moisture is mainly caused by the increase of the external adhesion layer. The particle size distribution of fluxes and iron ores is shown in Fig. 6, in which medium-sized particles with the particle size of 0.1–1 mm account for about 40% and 23%, respectively. There are relatively more large particles and fine powders in iron ore. Therefore, the increase of granulation moisture causes more flux particles to adhere to the external adhering layer. In the sintering process, the adhered medium-sized flux particles decompose and fully contact with the ore powder, so as to form a local high basicity area, resulting in a large amount and lower viscosity of liquid phase. So the gas flow resistance is smaller, conducive to the increase of gas flow rate, and easier to create gas flow channels [7]. This promotes the movement of bubbles in the molten liquid phase and the connection and coalescence, resulting in more open pores and less closed pores.

The proportion of the number of pores in different pore size ranges to the total number of pores in the high-temperature zone under different granulation moisture are shown in Figs. 7 and 8. The number of pores with the equivalent diameter of 0–0.2 mm accounts for the largest proportion of the total number of pores, consistent with Shatokha et al. [31]. Furthermore, there is little difference in pore number distribution under different granulation moisture.

It can be seen from Fig. 8 that with the increase of granulation moisture, the number of almost all of the pores increases except those with equivalent diameter + 1 mm, and the smaller the pores are, the more pronounced the increasing trend is. The flame front travels faster under high moisture, which means a shorter sintering time with a fixed bed height. Shorter time of high temperature in the bed leads to low melting and insufficient coagulation of materials. A large number of small bubbles cannot fuse into larger bubbles, thus leaving more small pores in the matrix. The number of pores with an equivalent diameter of + 1 mm does not show a significant trend with the change of granulation moisture, which may be because the larger pores are more affected by the structure of the green bed and air impact. The

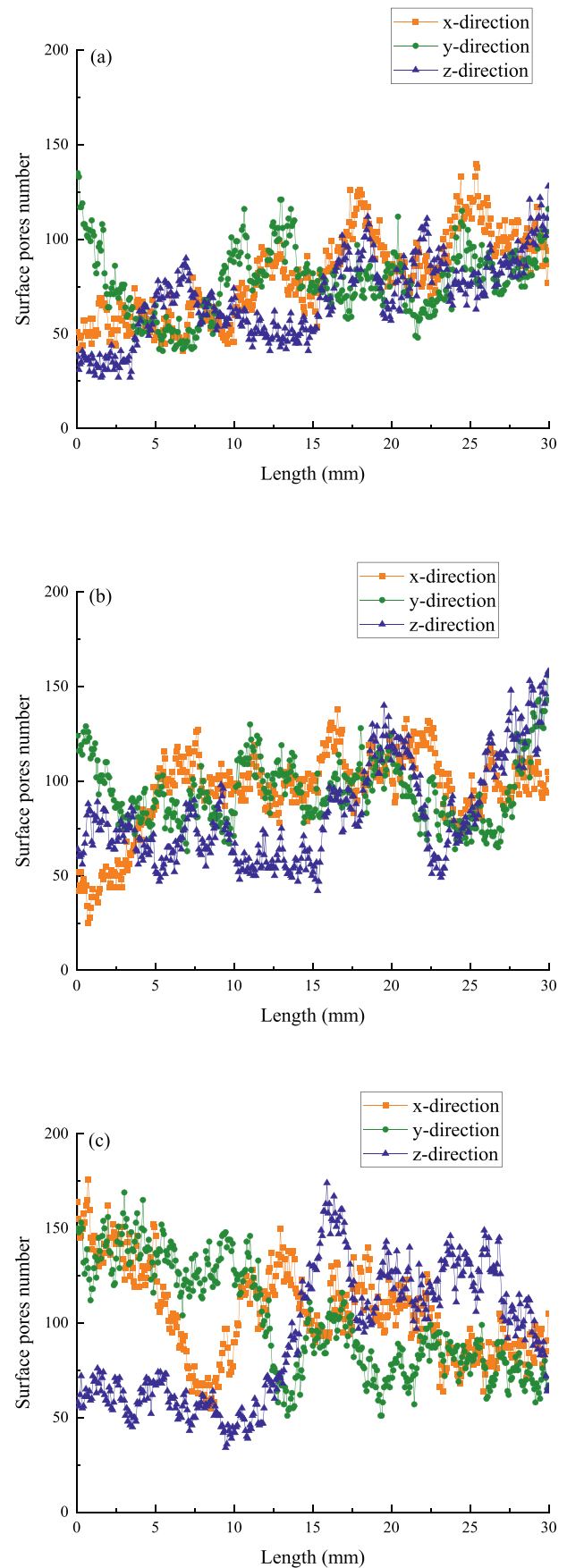


Fig. 12. Number of pores in different directions with different moisture, (a) 5.3%, (b) 6.35%, (c) 6.91%.

increase of green bed porosity and air impact is conducive to the formation of large pores. However, the bubble fusion caused by shorter sintering time is insufficient, which is not conducive to the formation of large pores. Under the superposition of the two effects, the number of large pores does not appear a noticeable change trend.

However, as shown in Fig. 9, granulation moisture did not significantly affect the volume fraction of pores with different pore diameters, which indicates that the increase of total pore volume is the result of the increase of pores in different particle size ranges. The volume fraction of pores with an equivalent diameter of +1 mm is high as 99%. These larger pores are more likely to fuse in the process of liquid phase flow in the high-temperature zone and form channels under the impact of gas flow, thus affecting the permeability of the high-temperature zone. It can be found that although the number of pores of −1 mm is large, their volume fraction is tiny combined with the results of Fig. 5. At high porosity, the proportion of small pore volume in the total pore volume remains unchanged, which indicates that the number of small pores increases significantly, which is consistent with the statistical results in Fig. 8, further proving that the pore fusion in the high-temperature zone is insufficient under high moisture. These micropores greatly influence the strength and reducibility of the sinter but little influence the gas flow resistance and thermal characteristics in the sintering process.

The sphericity of pores with different sizes in the high-temperature zone is shown in Fig. 10. It can be found that larger pores have smaller sphericity. The sphericity of 0–0.2 mm pores is about 0.38, while that of +1 mm pores is about 0.18. There is a three-phase fusion process of solid phase, melting and gas when the flame front arrives in the process of iron ore sintering, in which bubbles fuse and reshape, thus reducing the system energy. There are two opposite forces, surface tension and viscous force, affecting the reshaping process. The surface tension tends to make the bubble rounder, while the viscous force prevents this process [11]. The driving force of the reshaping process is a function of  $2\gamma/r$ , where  $\gamma$  is the surface tension of the melt and  $r$  is the bubble radius. Therefore, bubbles with small equivalent diameters are easier to reshape to near-spherical shape, which has the lowest system energy.

The gas flow impacts the liquid phase in the high-temperature zone from top to bottom during sintering, which coincides with the direction of gravity load. In order to explore whether the structure of the sinter is regular in spatial distribution, we took a certain number of sections equidistant in three directions of sinter samples, and made statistics on the face porosity and the pore number on each section. The data points in Figs. 11 and 12 correspond to the face porosity or the pore number on the section at a certain distance from the coordinate origin. If the pores in the high-temperature zone are regularly distributed in a certain direction, the curve in the figure will change according to a certain law. But as shown in Fig. 11, the change of face porosity in one direction is irregular, and there is no obvious difference in section porosity in different directions. The heterogeneity of the green bed

leads to the uneven distribution of pores in all directions. The number and size of pores are anisotropic in each direction. Vertical airflow impact and gravity load affect the remodeling of bed structure without changing the heterogeneity of pore space distribution.

In order to further understand the characteristics of the random distribution of these pores, the total amount of pores in different directions is analyzed, as shown in Fig. 12. In Fig. 12(c), the number of pores in different sections changes more violently and the variation range is significantly wider, indicating that the heterogeneity of pore number in each direction gets evident with the increase of moisture. With the increase of moisture, a shorter sintering time will reduce the combustion efficiency of coke and reduce the heat release of fuel [25,42]. The porosity and permeability of the sintering bed are higher, which means that the convective heat transfer is more intense after the air enters the bed. The gas flow will take more heat away, weakening the heat storage effect of the fixed packed bed.

The sintering bed can be divided into drying region, equilibrium zone, condensation zone and unreacted zone before the flame front reaches the bed from the perspective of moisture transfer [27]. As the flame front approaches the bed gradually, the water vapor carried by the sintering flow condenses in the unreacted zone, and the unreacted zone transforms into the condensation zone. As the flame front gets close, the condensation of water vapor and evaporation of water in the condensation zone reach a dynamic equilibrium, and the bed layer transforms into the equilibrium zone. The water in the bed evaporates rapidly when the flame front is coming, and the bed layer transforms into the drying region. Under the high moisture condition, the gas flow is faster, easier to take away the heat released by steam condensation in the condensation zone and the equilibrium zone, which also weakens the heat storage effect of the fixed packed bed. In addition, higher moisture content leads to more heat consumption for water evaporation in the process of transforming the equilibrium zone into the drying region, which reduces the bed temperature. The decrease of sintering bed temperature will lead to less liquid formation and worse liquid fluidity [43]. Shorter sintering time and lower bed temperature lead to the insufficient agglomeration of materials and insufficient coalescence of bubbles in the high-temperature zone, which results in more obvious non-uniformity in the distribution of pore numbers in all directions. On the contrary, higher bed temperature and longer sintering time provide more liquid phase with good fluidity under low moisture conditions, which means the viscous force of gas-liquid interface is lower, and the driving force of bubble reshaping is stronger. In a longer reshaping time, the heterogeneity brought by the green bed is overcome to a certain extent.

### 3.3. Pore skeleton network and parameters

The pore skeleton network under different granulating water conditions is reconstructed to show the overall pore characteristics of the

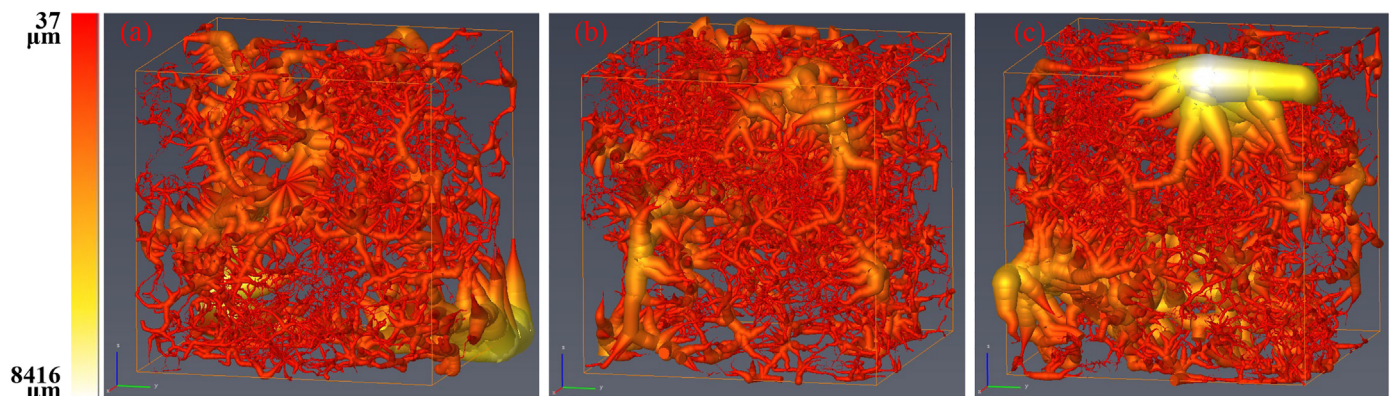
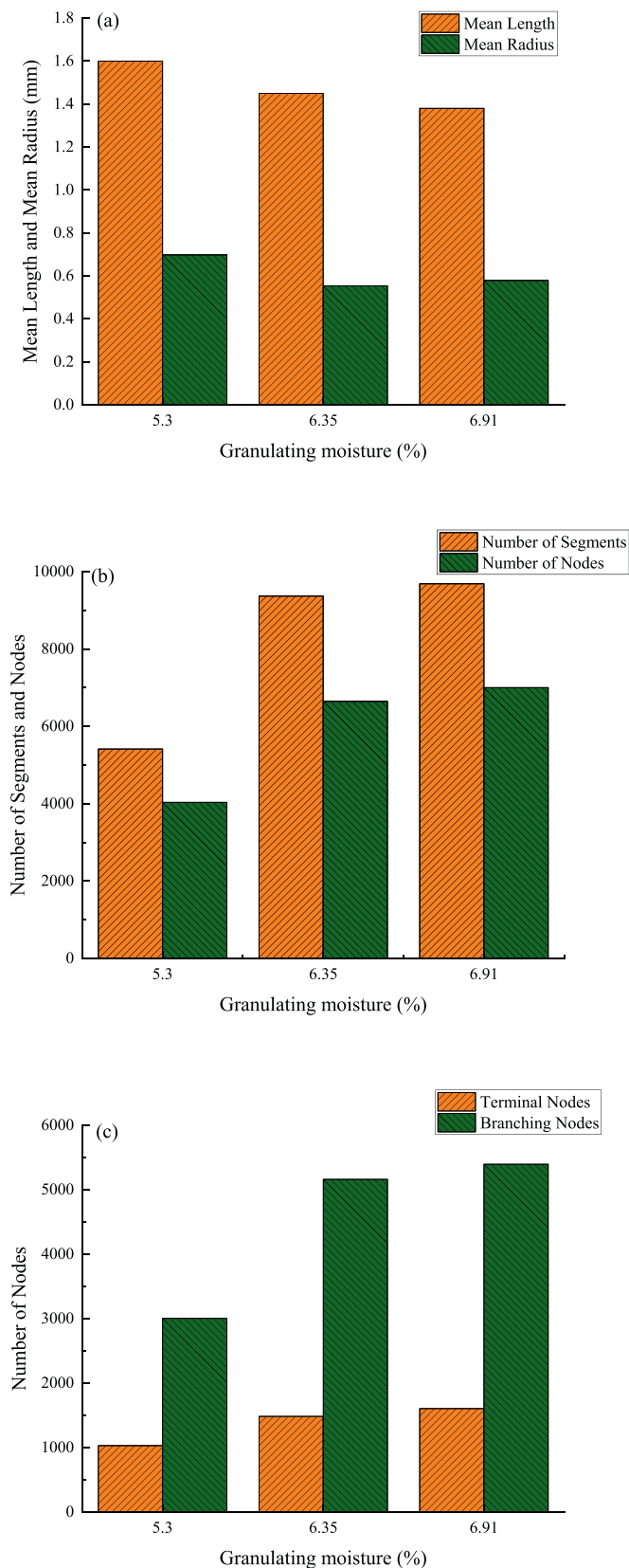


Fig. 13. Pore skeleton network with different moisture (a) 5.3%, (b) 6.35%, (c) 6.91%.



**Fig. 14.** Comparison of pore structure parameters with different moisture (a) mean length and radius of pores, (b) number of pore segments and nodes, (c) number of terminal nodes and branching nodes.

high-temperature zone intuitively, as shown in Fig. 13. It can be found that the distribution of pore networks under different moisture conditions is relatively random. The extraction of pore skeleton parameters is necessary for further study of the influence of granulation moisture on the characteristics of the pore skeleton.

The mean length and radius, the number of pore segments and nodes, and the number of terminal nodes and branching nodes of the high-temperature zone under different granulating moisture are shown in Fig. 14. Fig. 14(a) shows that the mean length of pores decreases from 1.60 mm to 1.45 mm and 1.38 mm with the increase of granulating moisture. The mean radius also appears a downward trend. While the segments and nodes, including terminal nodes and branching nodes, get more with the increase of moisture content, as shown in Fig. 14(b) and (c).

As discussed above, the lower the moisture content, the slower the flame front travels, contributing to a higher bed temperature and longer sintering time. The formation process of the sinter pore skeleton can be considered the integration and reshaping process of the green bed skeleton by gas flow impact, mass loss and material coalescence. Under low moisture content, sufficient material coalescence and bubble fusion are conducive to the extension and expansion of pores. In the process of bubbles extension, the nodes of two bubbles gradually contact and fuse to form a longer pore section. In the expansion process of a bubble made up of many branches, a trunk segment gradually expands and coarsens, merging with the smaller segments connected initially to form a coarser pore. Thus, the number of pore segments and nodes is less, and the developed pores are longer and coarser under low moisture conditions. However, the pore skeleton of the high-temperature zone is based on that of the green bed, after all. Under the condition of insufficient development, the pore skeleton is more limited by the green bed, so the pores will not be unlimited short and fine. In addition, the particle size of raw material is larger under high granulation moisture, so it is easy to form slightly larger pores in the packed bed. The above is why the mean radius of pores under 6.35% moisture and 6.91% moisture is not much different, as shown in Fig. 13(a).

#### 4. Conclusions

Due to the difficulty of sampling, the research on the pore morphology and distribution characteristics of the high-temperature zone of the sintering bed has been scarce. In this study, liquid nitrogen was introduced to quench the sintering bed, and X-ray computed tomography was used to reconstruct the three-dimensional structure of the high-temperature zone. We discussed the influence of granulation moisture on the flame front propagation characteristics and the pore characteristics in the high-temperature zone of the sintering bed by analyzing the pressure variation of the sintering bed, the pore distribution, and the pore skeleton parameters in the high-temperature zone. The main conclusions are as follows:

- (1) In the range of granulation moisture in this study, the flame front speed increases with the increase of granulation moisture, which mainly affects the pore structure and permeability of the green bed by affecting the particle size of granulation, thus affecting the permeability of the high-temperature zone.
- (2) The sphericity of pores is related to the relative magnitude of liquid surface tension and viscous force in the three-phase fusion process of solid phase, melting and bubble. The larger pores have smaller sphericity. The macropores with  $D_e$  larger than 1 mm account for about 10% of the total pores in number, but about 90% in volume, which play a leading role in gas flow resistance and thermal characteristics.

- (3) The increase of granulation moisture leads to short sintering time, low bed temperature, insufficient material coalescence and bubble fusion. More small pores and closed pores are formed in the high-temperature zone. The non-uniformity of pore distribution gets prominent.
- (4) Low bed temperature and short sintering time under high granulation moisture cannot make the pore framework reshape sufficiently. Many pores are not fully expanded, resulting in more pore segments and nodes are, while the mean radius and length get small.

### Declaration of Competing Interest

The authors declare no conflicts of interest.

### Acknowledgment

Funding: This work was supported by National Natural Science Foundation of China (52036008).

### References

- [1] D. Fernández-González, I. Ruiz-Bustanza, J. Mochón, C. González-Gasca, L.F. Verdeja, Iron ore sintering: process, *Miner. Process. Extr. Metall. Rev.* 38 (2017) 215–227, <https://doi.org/10.1080/08827508.2017.1288115>.
- [2] J.D. Litster, A.G. Waters, Kinetics of iron-ore sinter feed granulation, *Powder Technol.* 62 (1990) 125–134, [https://doi.org/10.1016/0032-5910\(90\)80075-a](https://doi.org/10.1016/0032-5910(90)80075-a).
- [3] A.A.M. Oliveira, M. Kaviany, Nonequilibrium in the transport of heat and reactants in combustion in porous media, *Prog. Energy Combust. Sci.* 27 (2001) 523–545, [https://doi.org/10.1016/S0360-1285\(00\)00030-7](https://doi.org/10.1016/S0360-1285(00)00030-7).
- [4] D. Liu, G. Evans, C.E. Loo, Iron ore sinter structure development under realistic thermal conditions, *Chem. Eng. Res. Des.* 130 (2018) 129–137, <https://doi.org/10.1016/j.cherd.2017.09.025>.
- [5] M.V. Ramos, E. Kasai, J. Kano, T. Nakamura, Numerical simulation model of the iron ore sintering process directly describing the agglomeration phenomenon of granules in the packed bed, *ISIJ Int.* 40 (2000) 448–454, <https://doi.org/10.2355/isijinternational.40.448>.
- [6] N. Oyama, T. Higuchi, S. Machida, H. Sato, K. Takeda, Effect of high-phosphorous iron ore distribution in quasi-particle on melt fluidity and sinter bed permeability during sintering, *ISIJ Int.* 49 (2009) 650–658, <https://doi.org/10.2355/isijinternational.49.650>.
- [7] H. Zhou, M. Zhou, P. Ma, M. Cheng, Experimental investigation on the flame front resistance of gas channel growth with melt formation in iron ore sinter beds, *Proc. Combust. Inst.* 37 (2019) 4607–4615, <https://doi.org/10.1016/j.proci.2018.09.027>.
- [8] C.E. Loo, J.C.M. Leaney, Characterizing the contribution of the high-temperature zone to iron ore sinter bed permeability, *Miner. Process. Ext. Metall.* 111 (2013) 11–17, <https://doi.org/10.1179/mpm.2002.111.1.11>.
- [9] B.G. Ellis, C.E. Loo, D. Witchard, Effect of ore properties on sinter bed permeability and strength, *Ironmak. Steelmak.* 34 (2013) 99–108, <https://doi.org/10.1179/174328107x165726>.
- [10] H. Zhou, M. Zhou, Z. Liu, M. Cheng, K. Qiu, K. Cen, Factors controlling high-temperature zone resistance to airflow during iron ore sintering, *ISIJ Int.* 55 (2015) 2556–2565, <https://doi.org/10.2355/isijinternational.ISIJINT-2015-311>.
- [11] C.E. Loo, W. Leung, Factors influencing the bonding phase structure of iron ore sinters, *ISIJ Int.* 43 (2003) 1393–1402, <https://doi.org/10.2355/isijinternational.43.1393>.
- [12] C.E. Loo, J. Heikkinen, Structural transformation of beds during iron ore sintering, *ISIJ Int.* 52 (2012) 2158–2167, <https://doi.org/10.2355/isijinternational.52.2158>.
- [13] J. Zhao, C.E. Loo, Dependence of flame front speed on iron ore sintering conditions, *Miner. Process. Ext. Metall.* 125 (2016) 165–171, <https://doi.org/10.1080/03719553.2016.1166565>.
- [14] H. Zhou, M. Zhou, M. Cheng, X. Guo, Y. Li, P. Ma, K. Cen, High resolution X-ray microtomography for the characterization of pore structure and effective thermal conductivity of iron ore sinter, *Appl. Therm. Eng.* 127 (2017) 508–516, <https://doi.org/10.1016/j.applthermaleng.2017.08.051>.
- [15] M. Zhou, H. Zhou, D.P. O’dea, B.G. Ellis, T. Honeyands, X. Guo, Characterization of granule structure and packed bed properties of iron ore sinter feeds that contain concentrate, *ISIJ Int.* 57 (2017) 1004–1011, <https://doi.org/10.2355/isijinternational.ISIJINT-2016-734>.
- [16] M. Zhou, J. Xu, H. Zhou, Evaluating the permeability properties of green bed in iron ore sintering using high resolution X-ray computed tomography and orthogonal array tests, *Powder Technol.* 375 (2020) 360–368, <https://doi.org/10.1016/j.powtec.2020.08.007>.
- [17] M.X. Zhou, H. Zhou, Evaluation of granule structure and strength properties of green packed beds in iron ore sintering using high-resolution X-ray tomography and uniaxial compression testing, *Particuology* 57 (2021) 157–166, <https://doi.org/10.1016/j.partic.2020.12.005>.
- [18] J. Xu, H. Zhou, M. Zhou, S. Hu, Y. Zuo, Taguchi orthogonal test on granule properties and porosity distribution in sintering bed using high-resolution X-ray computed tomography, *ISIJ Int.* 60 (2020) 1149–1158, <https://doi.org/10.2355/isijinternational.ISIJINT-2019-562>.
- [19] T. Inazumi, M. Fujimoto, S. Sato, K. Sato, Effect of sinter-charge load reduction by magnetic force on iron-ore sintering, *ISIJ Int.* 35 (1995) 372–379, <https://doi.org/10.2355/isijinternational.35.372>.
- [20] K. Higuchi, T. Kawaguchi, M. Kobayashi, Y. Hosotani, K. Nakamura, K. Iwamoto, M. Fujimoto, Improvement of productivity by stand-support sintering in commercial sintering machines, *ISIJ Int.* 40 (2000) 1188–1194, <https://doi.org/10.2355/isijinternational.40.1188>.
- [21] H.-b. Zuo, J.-l. Zhang, Z.-w. Hu, T.-j. Yang, Load reduction sintering for increasing productivity and decreasing fuel consumption, *Int. J. Miner. Metall. Mater.* 20 (2013) 131–137, <https://doi.org/10.1007/s12613-013-0704-9>.
- [22] H. Zhou, Z. Liu, M. Cheng, R. Liu, K. Cen, Effect of flame-front speed on the pisolite-ore sintering process, *Appl. Therm. Eng.* 75 (2015) 307–314, <https://doi.org/10.1016/j.applthermaleng.2014.09.050>.
- [23] H. Zhou, Z. Lai, L. Lv, H. Fang, H. Meng, M. Zhou, K. Cen, Improvement in the permeability of sintering beds by drying treatment after granulating sinter raw materials containing concentrates, *Adv. Powder Technol.* 31 (2020) 3297–3306, <https://doi.org/10.1016/j.apt.2020.06.017>.
- [24] C.E. Loo, A perspective of goethite ore sintering fundamentals, *ISIJ Int.* 45 (2005) 436–448, <https://doi.org/10.2355/isijinternational.45.436>.
- [25] H. Zhou, M. Zhou, M. Cheng, W. Guo, K. Cen, Experimental study and X-ray microtomography based CFD simulation for the characterization of pressure drop in sinter bed, *Appl. Therm. Eng.* 112 (2017) 811–819, <https://doi.org/10.1016/j.applthermaleng.2016.10.123>.
- [26] W.J. Rankin, P.W. Roller, Influence of water condensation on the permeability of sinter beds, *Trans. Iron Steel Inst. Jpn.* 27 (1987) 190–196, <https://doi.org/10.2355/isijinternational1966.27.190>.
- [27] A. Podder, Study of humidity on moisture transfer characteristics in iron ore sintering, *Trans. Indian Inst. Metals* 74 (2021) 1479–1487, <https://doi.org/10.1007/s12666-021-02244-3>.
- [28] J. Han, W. Sun, G. Pan, In situ dynamic XCT imaging of the microstructure evolution of cement mortar in accelerated carbonation reaction, *Mag. Concr. Res.* 64 (2012) 1025–1031, <https://doi.org/10.1680/mac.11.00173>.
- [29] S. Peng, Q. Hu, S. Dultz, M. Zhang, Using X-ray computed tomography in pore structure characterization for a Berea sandstone: resolution effect, *J. Hydrol.* 472–473 (2012) 254–261, <https://doi.org/10.1016/j.jhydrol.2012.09.034>.
- [30] K. Nushiro, N. Oyama, K. Igawa, Analysis of pore combination in sintering by hot stage X-ray computerized tomographic scanner, *ISIJ Int.* 39 (1999) 1239–1244, <https://doi.org/10.2355/isijinternational.39.1239>.
- [31] V. Shatkhia, I. Korobeynikov, E. Maire, L. Grémillard, J. Adrien, Iron ore sinter porosity characterisation with application of 3D X-ray tomography, *Ironmak. Steelmak.* 37 (2013) 313–319, <https://doi.org/10.1179/030192310x12683045805865>.
- [32] K.S. Augusto, S. Paciornik, Porosity characterization of iron ore pellets by X-ray microtomography, *Mater. Res. Ibero Am. J. Mater.* 21 (2018) <https://doi.org/10.1590/1980-5373-mr-2017-0621>.
- [33] M. Zhou, H. Zhou, Experimental investigation and numerical modeling of strength properties of iron ore sinter based on pilot-scale pot tests and X-ray computed tomography, *J. Mater. Res. Technol.* 9 (2020) 13106–13117, <https://doi.org/10.1016/j.jmrt.2020.09.054>.
- [34] T. Harvey, T. Honeyands, G. Evans, B. Godel, D. O’dea, Analogue iron ore sinter tablet structure using high resolution X-ray computed tomography, *Powder Technol.* 339 (2018) 81–89, <https://doi.org/10.1016/j.powtec.2018.07.098>.
- [35] J.P. Zhao, C.E. Loo, R.D. Dukino, Modelling fuel combustion in iron ore sintering, *Combust. Flame* 162 (2015) 1019–1034, <https://doi.org/10.1016/j.combustflame.2014.09.026>.
- [36] H. Zhou, M. Zhou, D.P. O’dea, B.G. Ellis, J. Chen, M. Cheng, Influence of binder dosage on granule structure and packed bed properties in iron ore sintering process, *ISIJ Int.* 56 (2016) 1920–1928, <https://doi.org/10.2355/isijinternational.ISIJINT-2016-298>.
- [37] M. Zhou, H. Zhou, D.P. O’dea, B.G. Ellis, T. Honeyands, X. Guo, Characterization of granule structure and packed bed properties of iron ore sinter feeds that contain concentrate, *ISIJ Int.* 57 (2017) 1004–1011, <https://doi.org/10.2355/isijinternational.ISIJINT-2016-734>.
- [38] T.R.C. Patrick, M.I. Pownceby, Stability of silico-ferrite of calcium and aluminum (SFCA) in air-solid solution limits between 1240 degrees C and 1390 degrees C and phase relationships within the Fe2O3-CaO-Al2O3-SiO2 (FCAS) system, *Metall. Mater. Trans. B Process Metall. Mater. Process. Sci.* 33 (2002) 79–89, <https://doi.org/10.1007/s11663-002-0088-0>.
- [39] M. Pownceby, J.J.M.P. Clout, Importance of fine ore chemical composition and high temperature phase relations: applications to iron ore sintering and pelletising, *E. Metall.* 112 (2003) 44–51, <https://doi.org/10.1179/037195503225011402>.
- [40] T. van den Berg, J. de Villiers, R. Cromarty, Variation of the redox conditions and the resultant phase assemblages during iron ore sintering, *Int. J. Miner. Process.* 150 (2016) 47–53, <https://doi.org/10.1016/j.minpro.2016.03.006>.
- [41] M. Zhou, H. Zhou, P. Ma, J. Xu, Effect of coke rate and basicity on computed tomography-measured pore parameters and effective thermal conductivity of iron ore sinter, *J. Mater. Res. Technol.* 8 (2019) 6191–6201, <https://doi.org/10.1016/j.jmrt.2019.10.013>.
- [42] C.E. Loo, N. Tame, G.C. Penny, Effect of iron ores and sintering conditions on flame front properties, *ISIJ Int.* 52 (2012) 967–976, <https://doi.org/10.2355/isijinternational.52.967>.
- [43] S. Wu, G. Zhang, S. Chen, B. Su, Influencing factors and effects of assimilation characteristic of iron ores in sintering process, *ISIJ Int.* 54 (2014) 582–588, <https://doi.org/10.2355/isijinternational.54.582>.